DESIGNING AND PROTOTYPING A SENSORS HEAD FOR TEST AND CERTIFICATION OF UAV COMPONENTS

Francesco Adamo*[a], Gregorio Andria [a], Attilio Di Nisio [a], Carlo Guarnieri Calò Carducci [a],
Aimé Lay-Ekuakille [b], Giuseppe Mattencini [a], Maurizio Spadavecchia [a]

[a]Electrical and Electronic Measurements Lab, Dept. of Electrical and Information
Engineering, Polytechnic University of Bari, Via Orabona 4, 70125 Bari, Italy
[b] Dept. of Innovation Engineering,
University of Salento, Centro Ecotekne Pal. O - S.P. 6, Lecce, Italy
*Correspondence: francesco.adamo @poliba.it; Tel.: +39-080-5963214

Abstract- The project proposed in this paper deals with the design and the development of an embedded test system able to characterize both electrical and mechanical performances of UAVs (Unmanned Aerial Vehicles) propulsion subsystems (motor and propeller). The measurement data that can be collected are of great interest for professional applications, as well as for amateur makers. Starting from the measures acquired by the presented system, it will be possible to deliver certificates that guarantee the customer that the performances obtained by the drone are compliant to what declared by the seller.

Index terms*: UAVs; propulsion; sensors; electric motors; test; certification.

I. INTRODUCTION

In the last few years, we have been assisting to the widespread utilization of small and medium size UAVs (Unmanned Aerial Vehicles), namely *drones*, and, in somewhat, *multicopters*. This is mainly a consequence of electronics and electrical technology advances and of the reduction of production costs of these devices. UAVs are used for several purposes, such as inspection of large infrastructures, surveillance, environmental monitoring, precision agriculture, rescue operations and news report [1] -[5].

It is not difficult to find, in both online and physical stores, drones capable to satisfy needs of professionals, scientists and authorities, as well as those of amateurs and hobbyists. Clearly, technical specifications of drones vary according to the intended application purposes. As an example, photographers and video makers have the necessity to capture high definition aerial images with the highest stability as possible, and very limited vibrations. Another aspect, to consider, is related to makers who want to build their own aero-models by buying and combining different components of the drone with the aim to obtain the highest performance with the lowest power consumptions, and, as a direct consequence, the longest flight autonomy. Research on UAVs is multidisciplinary and covers several topics such as control [5], mission management [7],[8], retreat in case of communication failure [9], and deployment of sensors [10]. Energy measurement, storage and management are of fundamental importance for UAVs flight [11]-[14]. Interestingly, vibrations of flying drones can be used to detect their presence and track them in open field [15]. Advances in sensor and imaging technologies pave the way to several UAV applications. It should be mentioned that thermography techniques, particularly suited to non-destructive testing and characterization of used materials, take advantage of the high spatial sampling capability of drones and find applications in the monitoring of industrial plants, buildings and energy production [16]-[19]. More in general, computer vision algorithms overcome the boundaries of laboratories and production chains and can be applied to real-time monitoring of large areas thanks to UAVs [20]-[24]. Similarly, applications of UAVs (both flying and submarine) to environmental monitoring and detection of pollutants have demonstrated their viability and integrated other approaches based on air pollutant models and geostatistical methodologies from stationary measurement stations [25]-[29]. Indeed, new optical sensors permit spectral analysis in the infrared, where many biological molecules and gases have a spectral fingerprint [31]-[36]. UAVs have the potential of being used for active and passive remote sensing [37]-[40].

Due to the variety of applications, it is noticeable the necessity of measuring the characteristics of the components of UAVs as well as whole UAVs, in order to assess their suitability for a given purpose [41]-[44]. Despite the abundance of literature on testing of aerospace materials and components [45]-[47], only few works have considered the problems of the UAV testing and of the design optimization for an assigned performance specification [48]-[51] and fewer have described also the measurement system [52], which is, instead, the focus of this paper.

The measurement system presented in this work is a test bench, aimed to UAV propelling subsystems, which can be used to correctly size and choose the components that give the desired performance. A suitable sensors head has been designed, which allows users to test and characterize a system consisting of an Electronic Speed Control (ESC), an electric motor and a propeller: this group of components is mounted on the sensors head of the test bench.

The proposed test bench is able to measure the following four quantities: the voltage applied to and the current absorbed by the propelling subsystem, the rotational speed of the motor, and the produced thrust. It has the peculiarity of integrating in a compact system the equivalent of several bench-top instruments, too.

The results obtained with the proposed measuring system can be used to choose the combination of ESCs, motors and propellers providing the best performance. Another foreseeable purpose of this system is to measure performance drifts and reliability of the ESCs and of the motors mounted on the drone. Indeed, by testing at regular intervals these two components, it is possible to determine the end of their life cycle and to reduce the risk of their failure during the flight time, which would lead to crashing the drone.

Finally, an important application of the presented test bench is certification. Indeed, this measurement system could be used by companies that produce or assemble UAVs to certify their devices, with respect to the expected performance specifications. The direct consequence of the certification process is the production of a legal document that guarantees the customer that the specific drone (or drone component) he bought is compliant to what declared by the seller or by the producer.

This paper is structured as follows. Sec. 2 explains the hardware architecture of the system and the design of the sensors head. Sec. 3 is centered on the software implementation of the test bench, including FPGA programming, control panel software and data acquisition software. In Sec. 4, the results obtained through the test bench are reported. In particular, the propulsion system of a F550 drone produced by *DJI* [53] has been tested and the results compared with those obtained with different laboratory instrumentation. Finally, Sec. 5 depicts a discussion of

the validity of the design on which the test bench is based and describes future improvements doable on this project.

II. SYSTEM ARCHITECTURE

The proposed measurement system includes three different sensors: i) a load cell to measure the thrust force exerted by the propeller; ii) an infrared reflective sensor to measure the rotational speed of the motor; and iii) a "power module" necessary to measure the voltage applied to the ESC and the absorbed current. Figure 1shows the sensors head of the prototype test bench.

The entire measuring system is controlled by a National Instruments' *myRIO®* embedded device [54], which is based on a Xilinx System-on-Chip (SoC) containing an ARM® Cortex™-A9 processor and a 28,000 cells programmable FPGA. It has been chosen because it provides many analog and digital inputs and outputs and is natively capable to control external hardware using several useful communication protocols: Inter Integrated Circuit (I^2C), Serial Peripheral Interface (SPI) and Universal Asynchronous Receiver-Transmitter (UART).

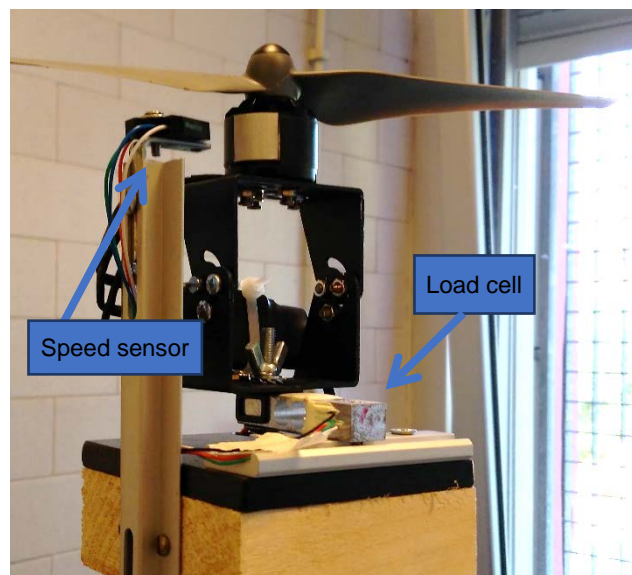The block diagram of the measurement system is depicted in Figure 2.

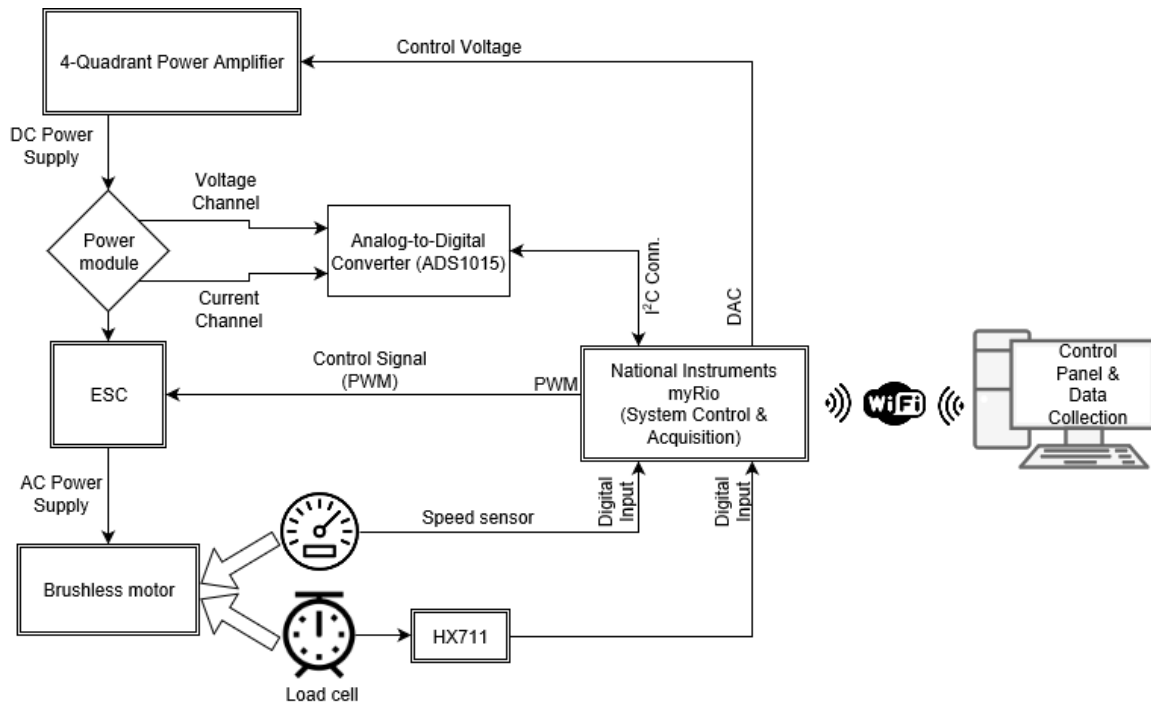
Figure 1. Sensors head of the measurement system.

Figure 2. Measurement system block diagram.

The NI *myRIO* represents the core of the system: it provides the driving voltage to the input of the 4-quadrant power amplifier and the PWM (Pulse Width Modulation) signal required by the ESC to control the rotational speed of the motor; it also collects all the outputs of the remaining sensors of the test bench which are connected to its digital inputs.

The propeller subsystem is powered by a Toellner's 4-quadrant power amplifier, model *TOE 7621-20* [55]; this device is used to emulate the behavior of a Lithium Polymers (Li-Po) battery of a drone. The output voltage of the amplifier is controlled by a low power voltage input delivered by a digital-to-analog converter (DAC) integrated in the *myRIO*. The voltage input/output gain of the 4-quadrant power amplifier is set to 4 V/V.

The rotational speed of the motor is regulated by the ESC, which has a digital input where a PWM signal is applied. The *throttle* (i.e. the power) of the motor is set through the duty-cycle of the PWM signal generated at one digital output of the *myRIO*.

The sensors used in the proposed measurement system are described in the following paragraphs.

a. Thrust force measurement

As shown in Figure 1, a load cell is mounted under the frame that retains the motor and the propeller; when the motor rotates, the propeller generates a vertical thrust force that is measured

by reading the voltage at the output of the load cell. Load cells, due to their high versatility and accuracy, have found a variety of applications, from monitoring of large structures to biomedical measurements[56]-[59]. In this work, a full Wheatstone's bridge configuration is used, where four strain gauges are mounted on the mechanical structure of the load cell, because it offers the best measurement accuracy. The output of the load cell is then conditioned and converted to digital by the AVIA Semiconductor's HX711 integrated circuit [60].

The HX711 has three main functional blocks: the first of them is a stable 1.25 V bandgap reference voltage circuit, used as the reference of an analog supply regulator, which in turn permits to obtain accurate readings even if different and fluctuating power sources are used. That analog supply provides excitation to the Wheatstone's bridge and, at the same time, powers the analog front-end and the analog-to-digital converter (ADC) of the HX711. The second block is necessary to filter, sample and convert to digital the analog value acquired from the output of the bridge; the ADC integrated into the HX711 is a 24-bit sigma-delta converter with a maximum conversion rate of 80 SPS (Samples per Second). The third and last functional block of the HX711 sends each converted value to the *myRIO* using a non-standard synchronous serial communication protocol.

An experimentally determined *calibration factor* is used to convert raw values read from the output of the HX711 into the *International System of Units*, typically to grams or Newton; it was determined by an accurate multi-point calibration process, based on a linear regression algorithm applied to measurements done on reference weights preliminarily measured with a calibrated high accuracy (ten thousandth of grams) weigh scale.

Each calibration point was measured 200 times and suitably averaged. In detail, 25 different calibration weights were applied first in growing order and then removed in decreasing order on the load cell; two linear least squares interpolations were performed to relate weight values to the ADC raw values. The result of this calibration is shown in Figure 3a; the sensor is highly linear in the range of interest with only a very limited deviation between the two calibration curves in the first portion of the range. The mean calibration curve has a slope of -137.92 LSB/g. Figure 3b shows the residuals between the mean calibration curve and the output codes, with a maximum of 250 LSB, corresponding to 1.81 g. For each calibration point, the standard deviation of 200 measurements was calculated, obtaining a maximum of 173.66 LSB, corresponding to 1.26 g.The force measurement system performs very well, despite its low cost.
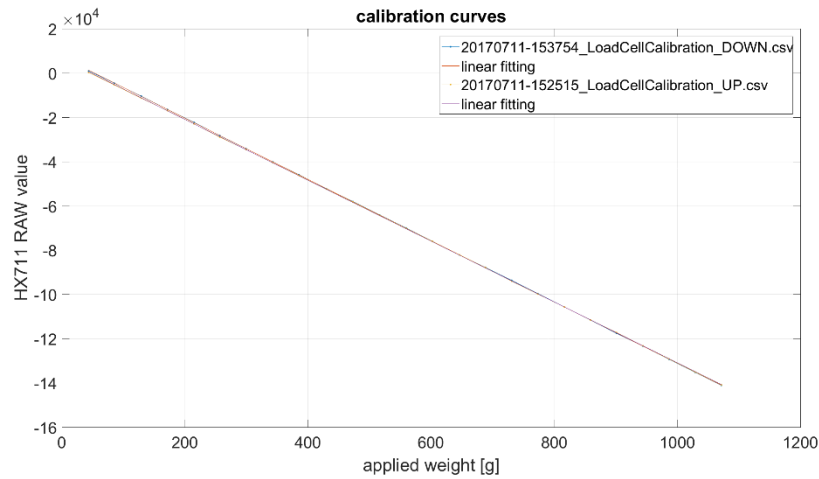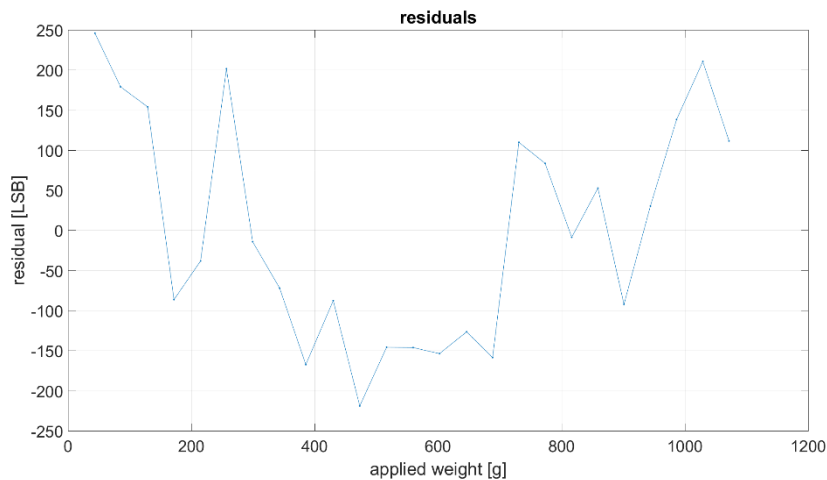
Figure 3. a) Linear regressions for load cell calibration and b) residuals of the regression.

As shown in Figure 1, the propulsion subsystem is mounted directly on the load cell in a vertical axis configuration; in detail, the only forces measured by the load cell are the thrust force and the force of gravity; however, the effect of the last one is zeroed during calibration. On the market, it is possible to find thrust meters based on the horizontal axis configuration; in this case, the propeller generates a thrust force that is orthogonal to the force of gravity. Specifically, the motor is fixed on a horizontal linear guide that is joined to the load cell. In this configuration, it is necessary to consider the effects of friction of the linear guide. This is not directly compensable by the system and it could affect thrust force measurements resulting, for example, in an apparent hysteresis when throttle is varied between a minimum and a maximum in a cycle. In conclusion, the vertical axis configuration was chosen to obtain more accurate thrust force measurements.
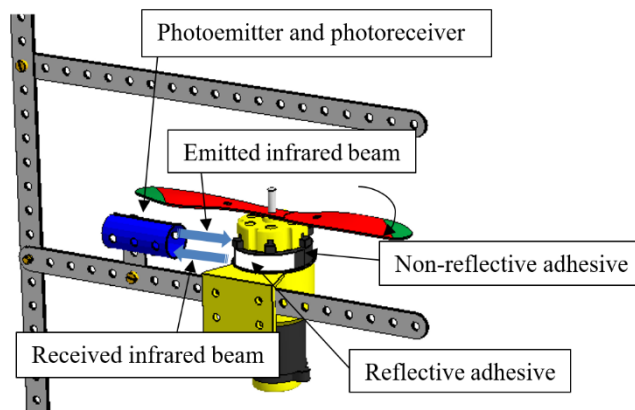
Figure 4.Scheme of rotational speed measurement for outrunner motors.

b. Rotational speed measurement

For outrunner motors, i.e. those with the external cage rotating, a reflective infrared sensor is mounted facing the rotating shell of the motor on which a small reflective tag is glued, as shown in Figure 4.

The infrared sensor, a QRB1134 by Fairchild Semiconductor [61], contains in a single molded package both the emitting diode and the photodetector; in this way, it is possible to simplify the physical implementation of the measuring system. The emitted light has a wavelength of 940 nm.

The emitted infrared beam is directed to the rotating shell of the motor on which two adhesives are applied: one of them is reflective (white), while the other one is non-reflective (black).

When the beam reaches the reflective adhesive, it returns to the photodetector, which provides a high voltage level on its output. On the other hand, when the beam arrives to the non-reflective adhesive, no appreciable reflection is produced because it is absorbed by the black adhesive. Therefore, the photodetector does not sense any infrared radiation, and provides a zero-voltage output. According to the data sheet, the ideal distance, between the sensor and the reflective adhesive, that produces the highest discrimination, is about 5 mm.

During the rotation of the motor, the photodetector outputs a square wave signal with frequency related to the speed of the motor by the equation:

$$f = N_R \cdot \frac{\omega}{60} \quad (Hz) \tag{1}$$

where: ω is the angular speed in *rpm* (revolutions per minute), and N_R is the number of reflective adhesives applied on the shell of the motor; in our case $N_R = 2$.
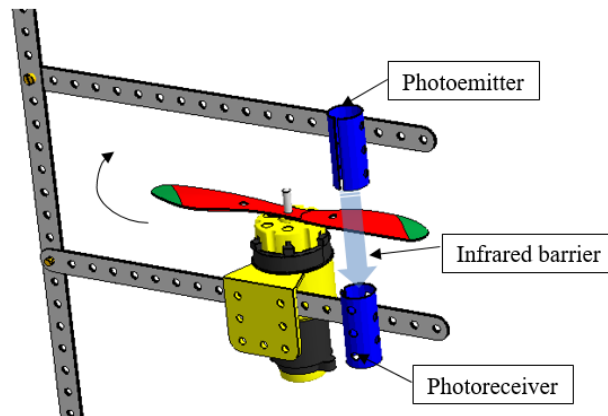
Figure 5. Scheme of rotational speed measurement for inrunner motors.

The output signal generated from the photodetector of the QRB1134 needs to be conditioned in order to give a reliable input to the digital pin of the *myRIO*; this is performed by a rail-to-rail threshold comparator which provides a high voltage on its output when the input voltage is above 2.5 V, and zero-voltage on its output when the input voltage is less than 2.5 V. Since the threshold of 2.5 V is determined by a resistive voltage divider, its real value is strictly related to the tolerance of the used resistors. Specifically, resistors with a tolerance of 1% are used.

Clearly, this setup is valid only outrunner motors; for *inrunner* motors, having a non-rotating external shell, an alternative setup which senses the passage of the rotating propeller trough an infrared beam has been designed and experimented (Figure 5).

In this case, the photoemitter, a *GL381 [62]* with peak wavelength of 950 nm, and the photoreceiver, *IS471F*[63] with peak wavelength of 940 nm, both manufactured by Sharp Corporation, are not encapsulated together in a single package, but are mounted in a vertical configuration in order to generate an infrared barrier that senses the crossing of the propeller blades. When the motor spins, the propeller blades periodically cross the infrared barrier; consequently, the output signal measured at the output of the photoreceiver resembles a square wave. In this case, the rotational speed of the motor is $\omega = 60 \cdot f / N_B$ (rpm), where f is the frequency of the square wave signal, expressed in hertz, and N_B is the number of bladesof the propeller. It is necessary to underline an interesting feature of the speed meter based on the IS471F photoreceiver. With the aim of increase immunity to external light disturbances, this IC outputs also a modulated signal driving the photo emitter, with a central frequency of 7.692 kHz. Accordingly, the received beam, sensed by the photoreceiver, is internally demodulated in the baseband and the obtained output signal is thresholded by a comparator internal to the

IC. As a result, the photoreceiver is immune to continuous external light disturbances up to 7500 lux at 940 nm.

c. Voltage and current measurements

The power module is a voltage and current measurement subsystem connected in series between the output of the 4-quadrant power amplifier and the power input of the ESC. A common power module compatible with APM 2.5 flight controllers has been used.

Voltage measurements are obtained using a voltage divider configured with a ratio of 1:10, which is the ratio between the output of the power module and the voltage applied to the ESC. The accuracy of the resistors of the divider should be as high as possible, because, the accuracy of measured voltages increases with the accuracy of resistors. In this specific case, the tolerance of each resistor is 0.1 %.

Current measurements are acquired, instead, through a shunt resistor method; this technique is implemented using a Texas Instruments *INA169*[64] in a high-side current sensing configuration. The shunt voltage is amplified by the INA169 with a gain set by both the transconductance gain of the integrated circuit and an external gain resistor.

The voltage V_O measured at the output terminal of the INA169 is related to the current I_S absorbed by the ESC through

$$V_O = R_S \cdot R_L \cdot g_m \cdot I_S, \tag{2}$$

where R_S is the shunt resistance, R_L is the external gain resistor and g_m is the transconductance. In the actual set-up, it is R_S= 0.5 mΩ, $R_L = 100$ kΩ and g_m=1000 µA/V, hence $V_O = 50\ m\Omega \cdot I_S$.

Measurements of I_S are also affected by resistor accuracies, in particular by the accuracies of the shunt resistor and of the gain resistor, and by the output error of the INA169. In this project R$_L$ and R$_S$ tolerances are both 0.1 % and the typical total output error of the INA169 is 0.5%.

The two analog outputs of the power module are then converted by a Texas Instruments *ADS1015* 12-bits sigma-delta with internal reference ADC [65]; two input configurations are possible: four multiplexed single-ended analog channels, or two multiplexed differential channels.

The communication between the ADS1015 and the *myRIO* is based on the I²C protocol.

Even though the *myRIO* includes a built-in ADC, we have preferred to use the external ADS1015 ADC, because the electrical specifications of the former do not meet the conversion requirements of the project. As a matter of fact, although the nominal resolutions of the two

ADCs are the same, the full-scale range of the integrated ADC in the *myRIO* is fixed to 10 V. This range is too large in comparison with the maximum voltages measurable at the output of the power module, which are 1 V for the current channel, and 2 V for the voltage channel. On the contrary, the ADS1015 allows to adjust its input full-scale range from the minimum value of 0.26 V to the maximum value of 6.14 V. This feature is useful to fully exploit the ADC resolution [66]-[67].

The current subsection of the power module was calibrated using a Yokogawa WT3000E Precision Power Analyzer as a reference for measuring the sourced current I_S, while a 6 ½ digits 34401A Keysight multimeter allowed us to measure the power module output V_O. 41 calibration points were used spanning from 0.03 A to 8 A. Actually, the current is controlled by setting the throttle of a motor from 0 % to 100 % in 2.5 % steps. The following relation was obtained by means of linear regression:

$$V_O = 0.0563 \cdot I_S + 0.0034 \quad (\text{V}). \tag{3}$$

In order to evaluate the accuracy of current measurement, new measurements were performed at the same nominal currents previously used during calibration by setting the same motor throttle values, so obtaining a total of 30 measurements for each calibration point. The RMS (Root Mean Squared) error between the measured current, obtained by inverting Eq. (3), and the calibration current is plotted in Figure 6. In that figure, the RMS error is calculated after aggregating measurements at the same throttle; it increases with current, up to about 0.04 A.
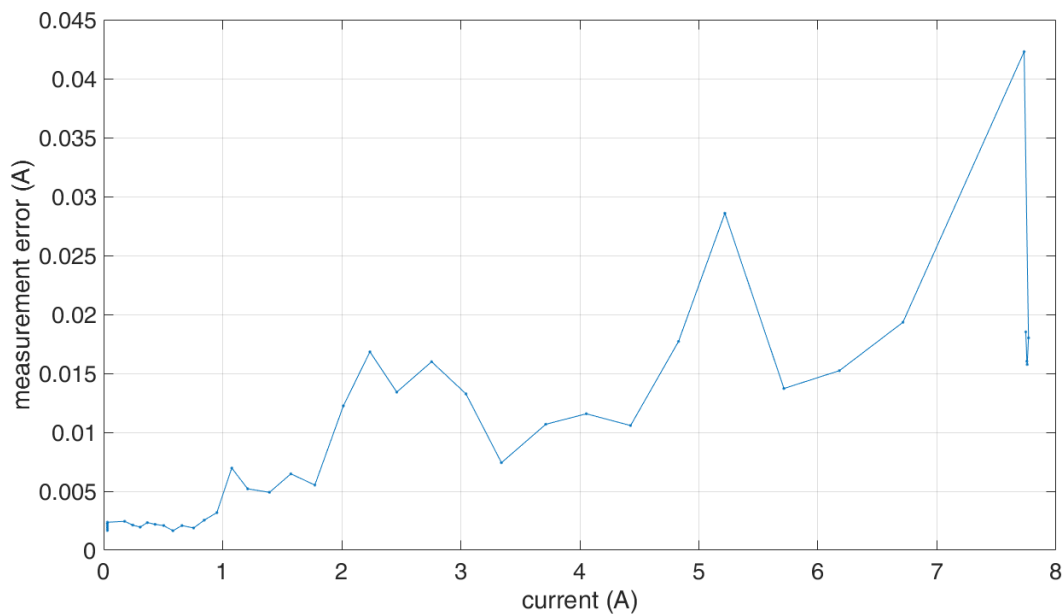

Figure 6. Error of measurement of current.

The calibration of the voltage measurement subsection of the power module proceeds analogously, hence it is not reported here for the sake of brevity.

III.   SOFTWARE DEVELOPMENT

The software that controls the system was entirely developed by the Authors in the well-known programming environment *National Instruments LabVIEW®*; it is composed by three main components: the *FPGA program* which gets data from the sensors and controls the actuators, the *User Interface VI*, which allows the user to control all the functions of the test bench, and the *Acquisition Panel* program, which permits to set all the parameters of the data acquisition system and to save the acquired characteristics in a *Comma Separated Values* (CSV) file. The last two programs run on the ARM processor of the *myRIO*.

a. FPGA program

The program running on the FPGA of the *myRIO*, is responsible of establishing the communication between the controller and each device of the test bench; it is totally independent from the other ones that run on the ARM processor of the *myRIO*. In this way, the FPGA is able to continuously acquire data from the sensors, and then to transmit them to the other programs only when they query for new data. The functions of the FPGA software are:

1. *Generation of the PWM control signal*. This signal is needed by the ESC in order to control the motor speed.

2. *Generation of the low power control voltage for the 4-quadrant power amplifier*. This voltage is generated at the output terminal of the DAC integrated in the *myRIO* and it is provided to the control input of the power amplifier.

3. Measurement of the frequency of the signal acquired from the infrared sensor.

4. *Reading of the output values from the HX711*. The FPGA reads the thrust force measurements from the output buffer of the HX711 and transmits them to higher lever VIs (Virtual Instruments) in raw format; conversions of the raw values to engineering units is performed by the ARM processor; this operation needs a scaling factor that is determined using results of the calibration procedure for the load cell.
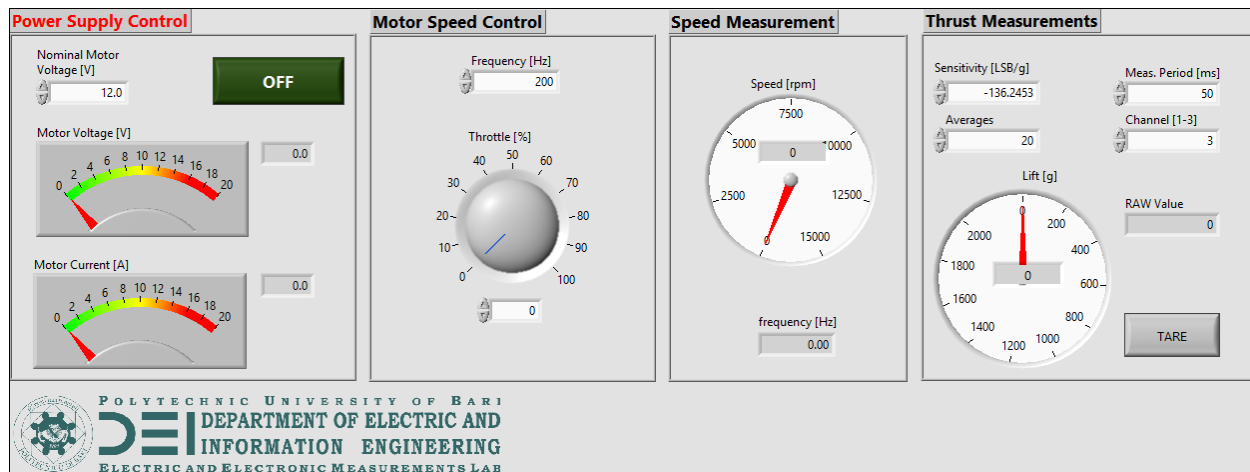
Figure 7. Control Panel of the test bench

5. *Reading of motor voltage and current*. The analog output signals of the power module are converted to digital by the Texas Instruments ADS1015 and transmitted to the *myRIO* using the I^{2}C protocol.

b. Control Panel

This software runs on the ARM processor of the *myRIO* and it lets users to control all sensors and actuators of the system (Figure 7).

The Control Panel is divided in four sections:

1. *Tachometer section for rotational speed measurement*: reads from the FPGA the frequency of the signal at the output of the infrared sensor; this value is then converted in rpm and showed on the gauge indicator of the visual interface.

2. *PWM control section*: allows users to set the desired values of duty-cycle and frequency of the PWM control signal at the input of the ESC.

3. *Thrust force measurement section*. The data transmitted by the HX711 and read by the FPGA are shown in this section; using this interface users can set both the calibration parameter, in order to convert raw values in engineering units, and the number *N* of readings to be averaged to improve measurement accuracy.

4. *Power section*. This part of the control panel includes two functions:
   i)   Control of the power supplied to the ESC. Beside the fine control of the output voltage, it is also possible to enable or disable the output of the 4-quadrant power amplifier.
   ii) Measurement of voltage and current supplied to the ESC.

In detail, the software of the control panel exploits the I^2C interface running on the FPGA to set the configuration register of the ADS1015 and to read the converted values from its conversion register.

c. Acquisition Panel

The Acquisition Panel (Figure 8) collects measurements of motor voltage, current, speed and thrust force for different values of throttle applied to the motor, show them on graphs during the test, and then saves them on a log file for further processing.

Before starting the acquisition cycle, users must set several parameters of the test: the throttle range and number of uniformly spaced sub values in it, the calibration factor of the load cell, the number of averaged thrust force measurements and the number of reflective adhesives applied to the shield of the motor.

At the end of the acquisition cycle, the software saves all the acquisitions into files in CSV format on the internal non-volatile memory of the myRIO; users interested to the post-processing of these data can open the files using MathWorks MATLAB® or Microsoft Excel. Each data file has a unique name based on execution date and time, so it is possible to collect many tests before downloading them from the myRIO memory.

The acquisition cycle is terminated clicking on the STOP button; this also removes power from the motor. Moreover, a hardware emergency button is present that permits to instantly switch off all power circuitry in the test bench.
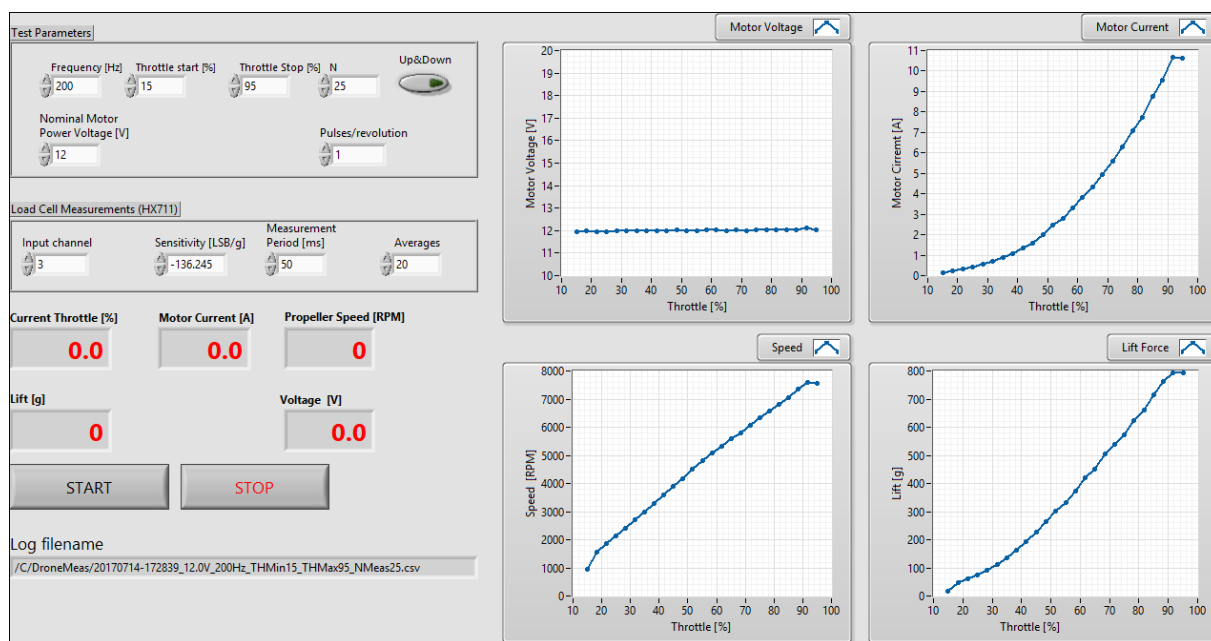

Figure 8. Acquisition Panel of the test bench

IV.   RESULTS

The propulsion subsystem of the DJI Flame Wheel F550 drone has been characterized using the proposed test bench; it is composed as follows: a synchronous outrunner three-phase brushless motor model DJI 2212 with Kv = 920 rpm/V [68], an ESC model DJI OPTO-E300 [69] and a 9443 carbon fiber reinforced propeller (diameter = 9.4 inches and pitch = 4.3 inches). The voltage applied to the ESC by the 4-quadrant amplifier was12 V, the frequency of the ESC control signal was $f_{PWM} = 200$ Hz and the throttle was spanned from 10% to 95%. From data reported in the motor data-sheet, the following relationship between the throttle r and the duty-cycle δ_{PWM} was estimated:

$$r = \frac{\frac{\delta_{PWM}}{f_{PWM}} - 1 \text{ ms}}{1 \text{ ms}} \Leftrightarrow \delta_{PWM} = (1 + r) \cdot f \cdot 10^{-3} \tag{4}$$

In order to reduce the effects of noise on the measured thrust force, for each applied throttle value the VI acquires and averages 20 measurements; the measured quantities are graphed in the following figures as function of the throttle value in percent. The standard deviations, calculated on 20 measurements, are displayed as bars.

Figure 9 shows the power supply output voltage; a voltage dropout of about 0.5 V is observed at maximum throttle. In this experimentation, a laboratory power amplifier has been used but, in general, measuring the voltage drop is useful when drone batteries are used under high-load conditions. Standard deviation increases up to 0.05 V for higher voltages.
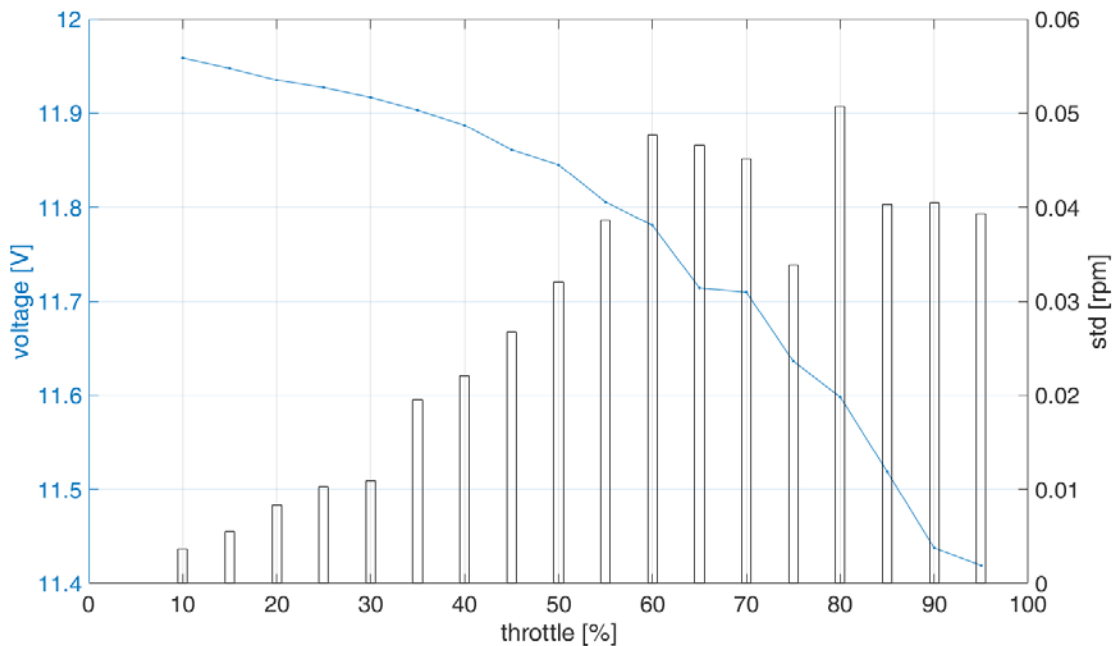

Figure 9. Voltage drop.

The current characteristic is reported in Figure 10, which shows that at full motor throttle the current absorbed by ESC and motor is slightly larger than 7 A; when the motor is stopped, the measured current is about 0.15 A, due to the quiescent power absorbed by the ESC. Maximum standard deviation is 0.11 A.

The maximum thrust generated by the chosen combination of motor and propeller is about 1.14 kg (11.2 N), as shown in Figure 11. Standard deviation increases with thrust up to about 20 g. Rotation speed is illustrated in Figure 12; maximum speed is around 8000 rpm. Standard deviation is higher at the extrema of throttle, where rotation can be affected by ESC effective operating range; its value, averaged over all throttle conditions, is 12 rpm. The results of the rotation speed measurement system have been compared with datasheet information. In particular, for a 12 V supply voltage, the rotational speed of the motor is 11129 rpm when the propeller is dismounted (no-load conditions), corresponding to 927 rpm/V; this result matches well with the nominal value 920 rpm/V reported on the datasheet [68].
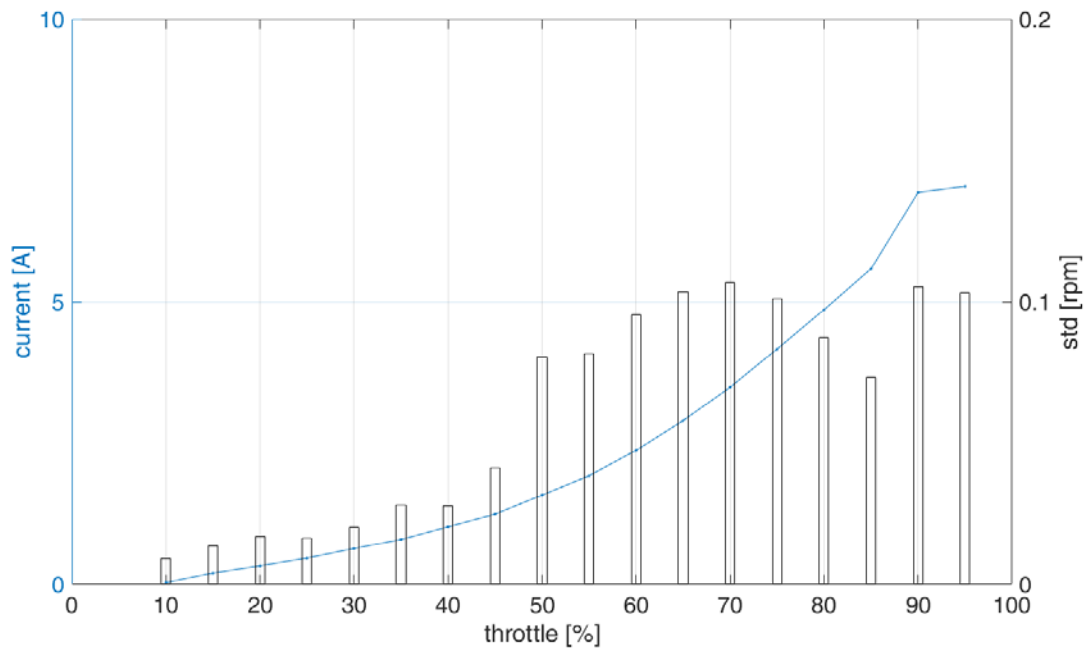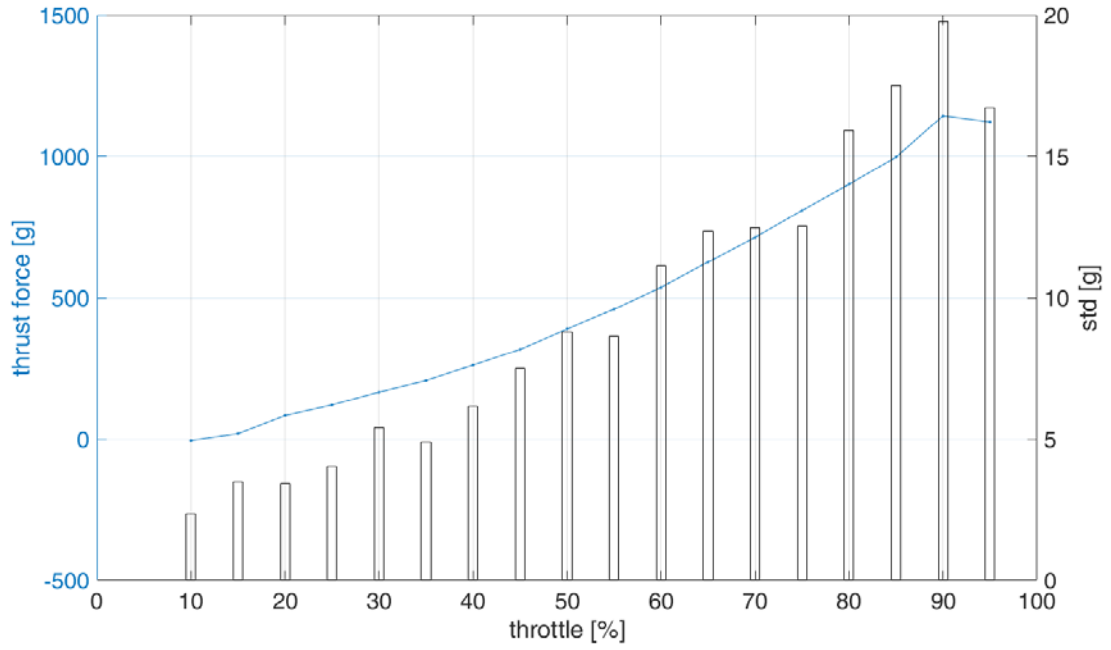

Figure 10. Current characteristic.

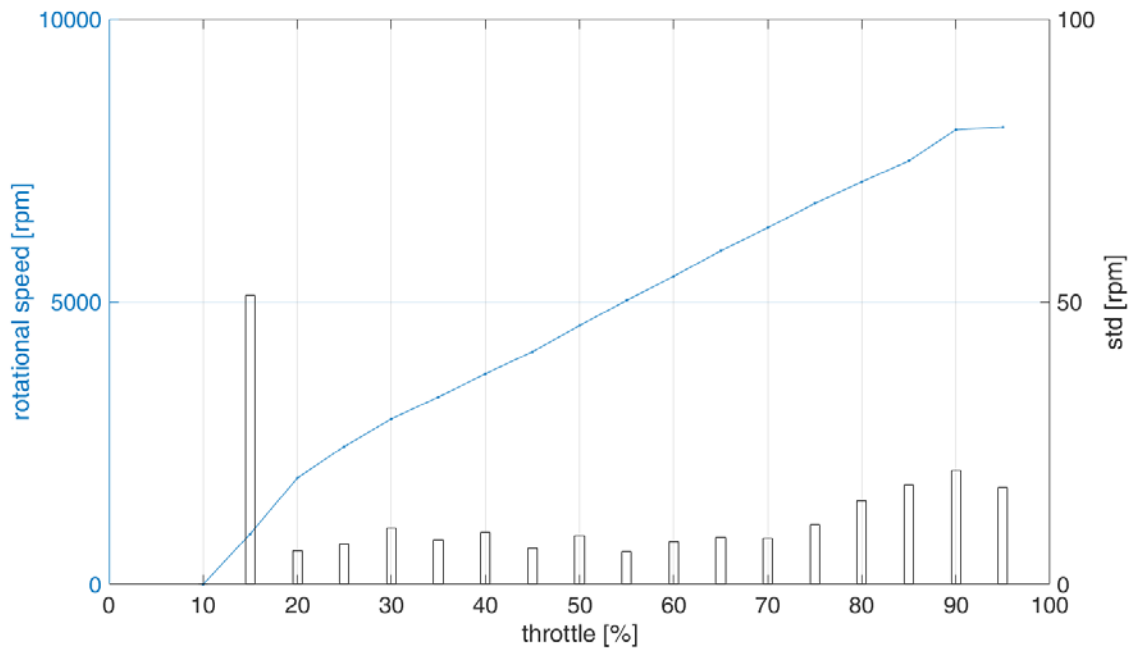**Figure 11**.Thrust characteristic.

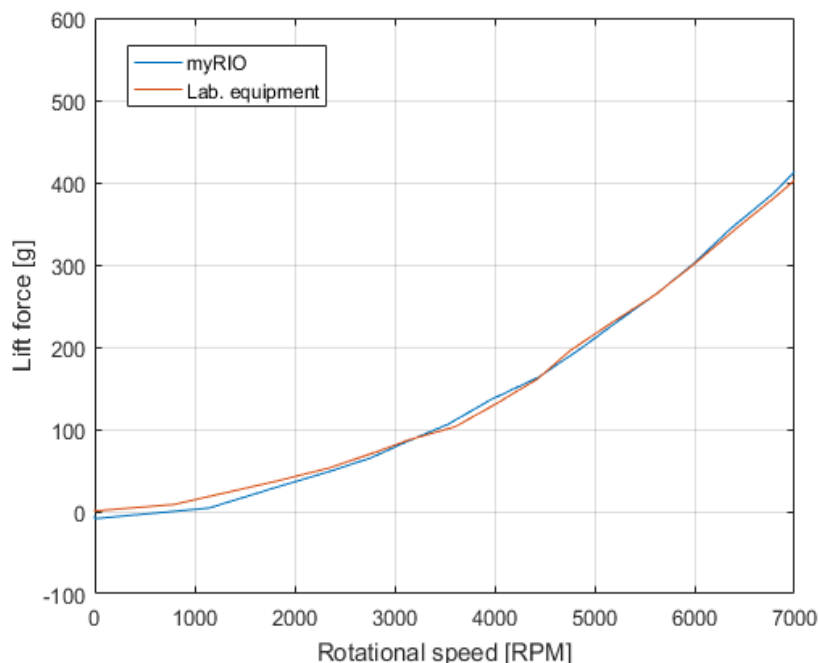
Figure 12. Speed characteristic.

Figure 13. Rotational speed vs. thrust force for the propulsion subsystem under test: (red) data measured with precision laboratory instrumentation, and (blue) data obtained with the integrated system based on *myRIO*.

In order to verify the correct operation of the system, a different sensor read-out system based on a precision GPIB-controlled bench-top instrumentation was used, in which the load cell and the power module outputs were digitized by a 6 ½ digits 34401A Keysight multimeter, the power amplifier input was provided by a Keysight E3631A power supply and the PWM signal to the ESC PWM was generated by a Keysight 33220A Arbitrary Waveform Generator. Figure 13 shows a comparison of the rotational speed vs. thrust force characteristics for the same propulsion subsystem measured with the two setups; the results are in good agreement, validating the design of the embedded measuring system.

Observing the previous graph, it is possible to relate the rotational speed of the propeller with the thrust force, which is useful since it allows to characterize propeller performance independently from the power supply and the specific model of motor on which the propeller is mounted. For example, propellers having the same length but different pitch will produce different thrust force at the same rotational speed.

The propeller under test (reinforced carbon fiber), here denoted as propeller "A", was compared with a propeller of same diameter (9.4 inches) and pitch (4.3 inches), but made of common plastic material and having a slightly different geometry, identified as propeller "B". Both propellers are depicted in Figure 14. During the test, a cycle was performed in which the throttle is increased from 0 % to 100 %, then it is decreased to 0 %, for a total of 40 test points. Each

point is the average of 19 measurements for both propellers. The results are reported in Figs. 15 and 16. The test cycles display a low hysteresis. It is noted that, at equal throttle settings, the reinforced carbon fiber propeller has higher speed, however the thrust is smaller. Maximum thrust difference is 112 g, about 10 %.

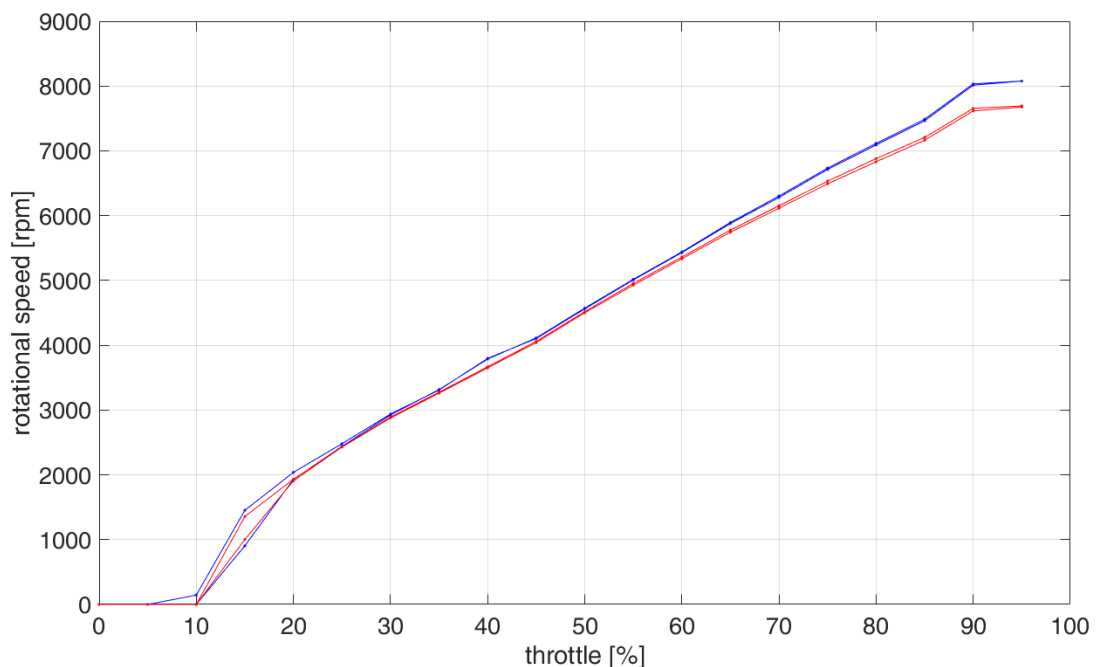**Figure 14**. Propeller "A" (top) and "B" (bottom).

Figure 15. Comparison of rotational speed between acarbon fiber reinforced propeller (blue line) and a common propeller (red line).
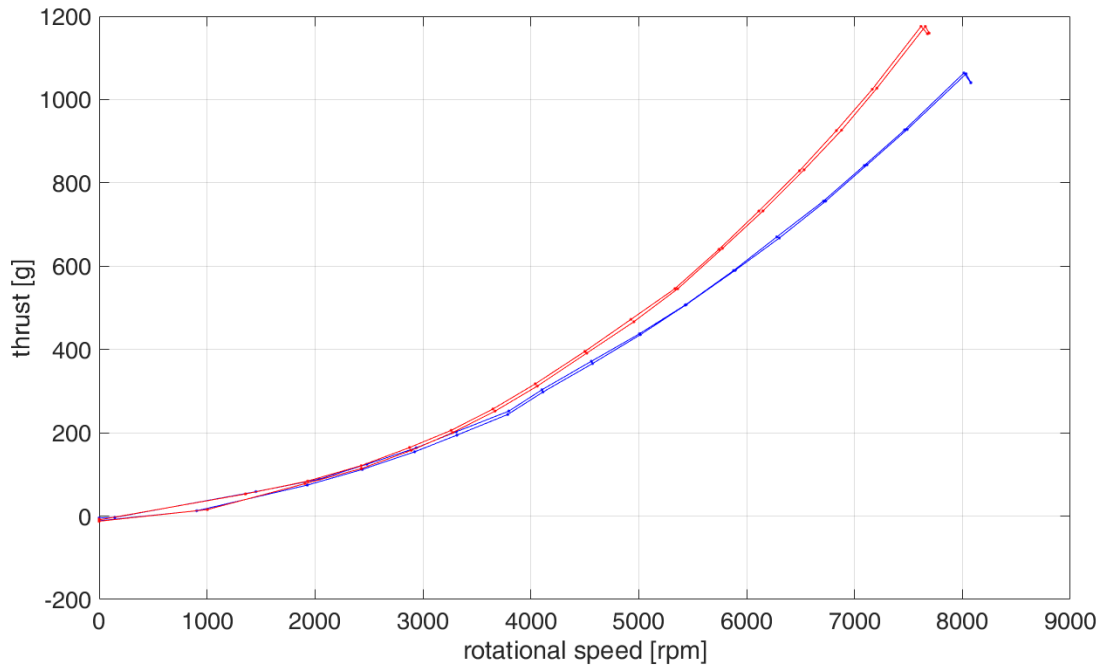
Figure 16. Comparison of thrust between a carbon fiber reinforced propeller (blue line) and a common propeller (red line).

V.   CONCLUSIONS

In this paper, a test bench for measuring the performance of drone propulsion systems has been presented. As shown in Figure 12, the results acquired with the integrated test bench based on the National Instruments *myRIO* are compatible with the ones obtained using more expensive laboratory instrumentation. The calibration procedure of the system has been illustrated, and repeatability results have been reported, which illustrate several aspects of measurement system performance. The force measurement system showed to be accurate despite its low cost.

Results of the characterization of two propellers have been reported, showing the relatively large difference of thrust, about 10%, despite their similarity in overall size. As expected, airfoil differences can produce large thrust variations, which stresses the importance of accurately characterizing and choosing the components of the propulsion system.

It should be noted that the availability of a large number of inputs on the *myRIO* and its small weight and dimensions allow users to integrate a larger number of sensors; this permits to parallelize the performance measures on all the motors and the propeller aboard a drone. As a matter of fact, it could be possible to provide each propulsion subsystem of the UAV with a voltage and current monitor, a rotational speed meter, and a load cell for thrust force measurement. In this way, the test duration can be significantly reduced and other kinds of tests

could be performed. For example, measuring at the same time the electrical and the mechanical performance characteristics of all the motors and the propellers of a drone, mismatches and drifts can be detected, which would otherwise lead to inefficiency or instability of the drone. The approach is considered necessary for safeguarding safety and performances during remote sensing in environmental and land monitoring as a simple example [66],[67].

REFERENCES

[1]   S. N. Ghazbi, Y. Aghli, M. Alimohammadi, A. A. Akbari, "Quadrotors Unmanned Aerial Vehicles: A Review", International Journal on Smart Sensing & Intelligent Systems, Vol. 9, no. 1, March 2016, pp. 309-333.

[2]   G. Pajares, "Overview and current status of remote sensing applications based on unmanned aerial vehicles (UAVs)", Photogrammetric Eng. & Remote Sensing, vol. 81, 2015, pp. 281-329.

[3]   A. Rango et al., "Unmanned aerial vehicle-based remote sensing for rangeland assessment, monitoring, and management", J. Appl. Remote Sensing, vol. 3, 2009, pp. 033542-033542-15.

[4]   G. J. Grenzdörffer, A. Engel, B. Teichert, "The photogrammetric potential of low-cost UAVs in forestry and agriculture", in The International Archives of the Photogrammetry, Remote Sensing and Spatial Information Sciences, Beijing, vol. 31, 2008, pp. 1207-1214.

[5]   A.E. Holton, S. Lawson, C. Love, "Unmanned Aerial Vehicles: Opportunities, barriers, and the future of drone journalism", J. Journalism Practice, vol. 9, 2015, pp. 634-650.

[6]   Y. Li, C. Chen, W. Chen, "Research on Longitudinal Control Algorithm for Flying Wing UAV Based on LQR Technology, International Journal on Smart Sensing & Intelligent Systems, Vol. 6, no. 5, December 2013, pp. 2155-2181.

[7]   S. Kyristsis, A. Antonopoulos, T. Chanialakis, E. Stefanakis, C. Linardos, A. Tripolitsiotis, P. Partsinevelos, "Towards Autonomous Modular UAV Missions: The Detection, Geo-Location and Landing Paradigm", Sensors, vol. 16, no. 11: 1844, 2016.

[8]   G. Yu, H. Song. J. Gao, "Unmanned Aerial Vehicle Path Planning Based on TLBO Algorithm", International Journal on Smart Sensing & Intelligent Systems, Vol. 7, no. 3, December 2014, pp. 1310-1325

[9]   J. Kang, Y. Kwon, K. Park, "Cooperative Spatial Retreat for Resilient Drone Networks", Sensors, vol. 17, no. 5:1018, 2017.

[10]   L. Sørensen, L. Jacobsen, J. Hansen, "Low Cost and Flexible UAV Deployment of Sensors", Sensors, vol. 17, no. 1:154, 2017.

[11]   E. M. Kwon, K. H. Yu, M. J. Yoon, G. Y. Jeong, G.Y, "Design considerations and modeling of a small and low altitude solar powered UAV", in Proceedings of 11th International Conference on Control, Automation and Systems, Gyeonggi-do, South Korea, 2011, pp. 1085-1088.

[12]   S. Sotheara, K. Aso, N. Aomi, S. Shimamoto, "Effective data gathering and energy efficient communication protocol in Wireless Sensor Networks employing UAV", in Proceedings of IEEE Wireless Communications and Networking Conference (WCNC), Istanbul, Turkey, 6-9 April 2014, pp. 2342-2347.

[13]   A. Di Nisio, T. Di Noia, C. Guarnieri Calò Carducci, M. Spadavecchia, "High dynamic range power consumption measurement in microcontroller-based applications", IEEE Trans. Instr. Meas. no. 65, 2016, pp. 1968-1976.

[14]   G.P. Kladis, et al. "Energy conservation based fuzzy tracking for unmanned aerial vehicle missions under a priori known wind information", Engineering Applications of Artificial Intelligence, vol. 24, 2011, pp. 278-294.

[15]   M. Jiang, T. Aoyama, T. Takaki, I. Ishii, "Pixel-Level and Robust Vibration Source Sensing in High-Frame-Rate Video Analysis", Sensors vol. 16, no. 11:1842, 2016.

[16]   L. E. Mavromatidis et al., "First experiments for the diagnosis and thermophysical sampling using impulse IR thermography from Unmanned Aerial Vehicle (UAV)", in Proceedings of QIRT Conf., Bordeaux, France, July 2014, pp. 1-8.

[17]   M. Dalsass et al., "Correlation between the generated string powers of a photovoltaic: Power plant and module defects detected by aerial thermography", in Proceedings of IEEE Photovoltaic Specialists Conference (PVSC), Portland, OR, 5-10 June 2016, pp. 3113-3118.

[18]   G. Andria, A.M.L Lanzolla, F. Piccininni, G.S. Virk, G.S., "Design and characterization of solar-assisted heating plant in domestic houses", IEEE Trans. Instr. Meas., vol. 57, 2008, pp. 2711-2719.

[19]   F. Attivissimo, A. Di Nisio, C. Guarnieri Calò Carducci, M. Spadavecchia, "Fast thermal characterization of thermoelectric modules using infrared camera", IEEE Trans. Instr. Meas., vol. 66, 2017, pp. 305-314.

[20]   H. Cruz, M. Eckert, J. Meneses, J. Martínez, "Efficient Forest Fire Detection Index for Application in Unmanned Aerial Systems (UASs)", Sensors, vol. 16, no. 6:893, 2016.

[21]   L. Evans, T. Jones, K. Pang, S. Saimin, B. Goossens, "Spatial Ecology of Estuarine Crocodile (Crocodylus porosus) Nesting in a Fragmented Landscape", Sensors, vol. 16, no. 9: 1527, 2016.

[22]   F. Adamo, F. Attivissimo, A. Di Nisio, M. Savino, "A low-cost inspection system for online defects assessment in satin glass", Measurement: Journal of the International Measurement Confederation, vol. 42, 2009, pp. 1304-1311.

[23]   L. Hongguang, D. Wenrui, W. Yufeng, "Three-Step Registration and Multi-Thread Processing Based Image Mosaic for Unmanned Aerial Vehicle Applications", International Journal on Smart Sensing & Intelligent Systems, Vol. 9, no. 2, June 2016, pp. 1090-1109

[24]   F. Adamo, F. Attivissimo, A. Di Nisio, M. Savino, "An online defects inspection system for satin glass based on machine vision", in Proceedings of IEEE Intrumentation and Measurement Technology Conference, I2MTC, Singapore, 5-7 May 2009, pp. 288-293.

[25]   K. Weber et al., "The use of an octocopter UAV for the determination of air pollutants– a case study of the traffic induced pollution plume around a river bridge in Duesseldorf, Germany", International Journal of Environmental Science, vol. 2, 2017, pp 63-68.

[26]   Y. Lu et al., "A UAV-mounted whole cell biosensor system for environmental monitoring applications", IEEE transactions on nanobioscience, vol. 14, 2015, pp. 811-817.

[27]   G. Andria, G. Cavone, V. Di Lecce, A.M.L. Lanzolla, "Model characterization in measurements of environmental pollutants via data correlation of sensor outputs", IEEE Trans. Instr. Meas., vol. 54, 2005, pp. 1061-1066.

[28]   V. Pelillo, L. Piper, A. Lay-Ekuakille, A. Lanzolla, G. Andria, R. Morello, "Geostatistical approach for validating contaminated soil measurements", Measurement: Journal of the International Measurement Confederation, vol. 47, 2014, pp. 1016-1023.

[29]   F. Giordano, G. Mattei, C. Parente, F. Peluso, R. Santamaria, "Integrating Sensors into a Marine Drone for Bathymetric 3D Surveys in Shallow Waters", Sensors, vol. 16, no. 1:41, 2016.

[30]   F. Adamo, F. Attivissimo, C. Guarnieri Calò Carducci, A.M.L. Lanzolla, A.M.L, "A smart sensor network for sea water quality monitoring", IEEE Sensors Journal, vol. 15, 2015, pp. 2514-2522.

[31]   I. Borra-Serrano, J. M. Peña, J. Torres-Sánchez, F. J. Mesas-Carrascosa, F. López-Granados, "Spatial Quality Evaluation of Resampled Unmanned Aerial Vehicle-Imagery for Weed Mapping", Sensors, vol. 15, 2015, pp. 19688-19708.

[32]   G. Palma et al., "Novel double step approach for optical sensing via microsphere WGM resonance", Optics Express, vol. 24, 2016, pp. 26956-26971.

[33]   S.L. Cundill, H.M.A van der Werff, M. van der Meijde, "Adjusting Spectral Indices for Spectral Response Function Differences of Very High Spatial Resolution Sensors Simulated from Field Spectra", Sensors, vol. 15, 2015, pp. 6221-6240.

[34]   J. Wojtas, A. Gluszek, A Hudzikowski, F.K. Tittel, "Mid-Infrared Trace Gas Sensor Technology Based on Intracavity Quartz-Enhanced Photoacoustic Spectroscopy", Sensors, vol. 17:513, 2017.

[35]   G. Palma, et al., "Modeling of whispering gallery modes for rare earth spectroscopic characterization", IEEE Photonics Technology Letters, vol. 27, 2015, pp. 1861-1863.

[36]   G. Palma, et al. "Design of praseodymium-doped chalcogenide micro-disk emitting at 4.7 µm", Optics Express, vol. 25, 2017, pp. 7014-7030.

[37]   S. Naumann, A. Siegmund, R. Ditter, M. Haspel, M. Jahn, and A. Siegmund. "Remote sensing in school–Theoretical concept and practical implementation" E-Learning Tools, Techniques and Applications, edited by G König & H Lehmann (ISPRS, Potsdam), 2009.

[38]   M. Jahn, M. Haspel, and A. Siegmund, "Using remote sensing data in the context of education for sustainable development," in Proc. of 30th EARSeL Symposium of Remote Sensing for Science, Educafion, and Natural and Cultural Heritage, 2010, pp. 731-738.

[39]   G. Andria, A. Baccigalupi, M. Borsic, P. Carbone, P. Daponte, C. De Capua, A. Ferrero, D. Grimaldi, N. Locci, A. M. L. Lanzolla, D. Macii, C. Muscas, L. Peretto, D. Petri, S. Rapuano, M. Riccio, S. Salicone, F. Stefan, "Remote Didactic Laboratory "G. Savastano: the Italian Experience for the E-learning at the Technical Universities in the Field of the Electrical and Electronics Measurements, Architecture and Optimization of the Communication Performance Based on Thin Client Technology", IEEE Transactions on Instrumentation and Measurement, ISSN:0018-9456, vol. 56, no. 4, August 2007, pp. 1124-1134.

[40]   G. Andria, A. Baccigalupi, M. Borsic, P. Carbone, P. Daponte, C. De Capua, A. Ferrero, D. Grimaldi, N. Locci, A. M. L. Lanzolla, D. Macii, C. Muscas, L. Peretto, D. Petri, S. Rapuano, M. Riccio, S. Salicone, F. Stefan, "Remote Didactic Laboratory "G. Savastano: the Italian Experience for the E-learning at the Technical Universities in the Field of the Electrical and Electronics Measurements, Overview on Didactic Experiments", IEEE Transactions on Instrumentation and Measurement, ISSN:0018-9456, vol. 56, no. 4, August 2007, pp. 1135-1147.

[41]   T. Mutlu, C. Hajiyev, "Flight tests, data collection, system identification, performance analysis of multicopter vehicle", in Proceedings of the 2014 6th International Conference on Electronics, Computers and Artificial Intelligence (ECAI), Bucharest, Romania, October 2014, pp. 19-26.

[42]   L. Derafa, T. Madani, A. Benallegue, "Dynamic modelling and experimental identification of four rotors helicopter parameters," 2006 IEEE International Conference on Industrial Technology, Mumbai, 2006, pp. 1834-1839.

[43]   N. V. Hoffer, C. Coopmans, A.M. Jensen, Y. Chen, "A Survey and Categorization of Small Low-Cost Unmanned Aerial Vehicle System Identification", J. Intell. Robotics Syst., vol. 74, 23-25 October 2014, pp. 129-145.

[44]   N.V. Hoffer, C. Coopmans, A.M. Jensen, Y. Chen, R.R. Fullmer, "Small low-cost unmanned aerial vehicle system identification: Brief sensor survey and data quality, consistency checking, and reconstruction", in Proceedings of International Conference on Unmanned Aircraft Systems (ICUAS), Orlando, FL, 2014, pp. 477-482.

[45]   P. López-Rodríguez, D. Escot-Bocanegra, D. Poyatos-Martínez, F. Weinmann, "Comparison of Metal-Backed Free-Space and Open-Ended Coaxial Probe Techniques for the Dielectric Characterization of Aeronautical Composites", Sensors, vol. 16, no. 7:967, 2016.

[46]   J. Gryzagoridis, D. Findeis, "Simultaneous shearographic and thermographic NDT of aerospace materials", Insight - Non-Destructive Testing and Condition Monitoring, vol. 48, 2006, pp. 294-297.

[47]   G. Andria, A. Di Nisio, V.L. Scarano, V.L., M. Spadavecchia, M. Bregoli, M. Franceschi, M., N. Tavernini, "Accelerated life tests of a new optocoupler for aerospace application", in Proceedings IEEE International Workshop on Metrology for Aerospace, MetroAeroSpace 2014, Benevemto, Italy, 29-30 May 2014, pp. 510-514.

[48]   Ø. Magnussen, G. Hovland, M. Ottestad, "Multicopter UAV design optimization", in Proceedings 2014 IEEE/ASME 10th International Conference on Mechatronic and Embedded Systems and Applications (MESA), Senigallia, Italy, 2014, pp. 1-6.

[49]   Ø. Magnussen, M. Ottestad, G. Hovland, "Multicopter design optimization and validation", Modeling, Identification and Control, vol. 36, 2015, pp. 67–79.

[50]   J.M. Winslow, V. Hrishikeshavan, I. Chopra, "Design Methodology for Small Scale Unmanned Quadrotors", in Proceedings 55th AIAA Aerospace Sciences Meeting, Grapevine, Texas, 9 - 13 January 2017, pp. 1-15.

[51]   W.A. Anemmat, et al., "Aerodynamic Design, Analysis and Testing of Propellers for Small Unmanned Aerial Vehicles", In Proceedings 55th AIAA Aerospace Sciences Meeting, Grapevine, Texas, 9-13 January 2017, pp. 1-12.

[52]   C.R. Russel, et al., "Wind Tunnel and Hover Performance Test Results for Multicopter UAS Vehicles", in Proceedings of AHS 72nd Annual Forum, West Palm Beach, FL, 16-19 May 2016, pp. 1-20.

[53] Dà-Jiāng Innovations Science and Technology Co. Ltd (DJI). Flame Wheel 550 (F550) specifications. Available online: https://www.dji.com/flame-wheel-arf/spec (accessed on 10 May 2017).

[54] National Instruments Corp., "myRIO-1900 User Guide and Specifications", Available online: http://www.ni.com/pdf/manuals/376047a.pdf (accessed on 10 May 2017).

[55] Toellner, TOE7621-20 4-Quadrant Power Supply specifications. Available online: http://www.toellner.de/html/img/pool/EN_7621.pdf (accessed on 10 May 2017).

[56] I. Muller, R. M. de Brito, C. E. Pereira, V. Brusamarello, "Load cells in force sensing analysis -- theory and a novel application", IEEE Instrumentation & Measurement Magazine, vol. 13, 2010, pp. 15-19.

[57] W. K. Lee, H. Yoon, C. Han, K. M. Joo, K. S. Park, "Physiological Signal Monitoring Bed for Infants Based on Load-Cell Sensors", Sensors, vol. 16, no. 3:409, 2016.

[58] G. Andria, F. Attivissimo, N. Giaquinto, A.M.L. Lanzolla, L. Quagliarella, N. Sasanelli, "Functional evaluation of handgrip signals for Parkinsonian patients", IEEE Trans. Instr. Meas., vol. 55, 2006, pp. 1467-1473.

[59] A. Blakeborough, D. Clément, M.S. Williams, N. Woodward, "Novel load cell for measuring axial force, shear force, and bending movement in large-scale structural experiments", Experimental Mechanics, vol. 42, 2002, pp. 115–122.

[60] Avia Semiconductor. HX711 - 24-Bit Analog-to-Digital Converter (ADC) for Weigh Scales. Available online: https://cdn.sparkfun.com/datasheets/Sensors/ForceFlex/hx711_english.pdf (accessed on 10 May 2017).

[61] Fairchild Semiconductor, QRB1134 - Phototransistor Reflective Object Sensors. Available online: http://courses.cs.washington.edu/courses/csep567/10wi/labs/QRB1134.pdf (accessed on 10 May 2017).

[62] Sharp Semiconductor, GL380/GL381 - High Output, φ 3mm Resin Mold Type Infrared Emitting Diode. Available online: http://pdf.datasheetcatalog.com/datasheet/Sharp/mXvqxzt.pdf (accessed on 10 May 2017).

[63] Sharp Semiconductor, IS471F - OPIC Light Detector with Built-in Signal Processing Circuit for Light Modulation System. Available online: http://courses.csail.mit.edu/6.141/spring2009/pub/labs/Grasping/docs/Breakbeam-Sensor-Sharp-IS471F.pdf (accessed on 10 May 2017).

[64]   Texas Instruments, INA139/169 - High-Side Measurement Current Shunt Monitor. Available online: https://cdn.sparkfun.com/datasheets/Sensors/Current/ina169.pdf (accessed on 10 May 2017).

[65]   Texas Instruments. ADS1015 - Ultra-Small, Low-Power, I2C-Compatible, 3.3-kSPS, 12-Bit ADCs With Internal Reference, Oscillator, and Programmable Comparator. Available online: http://www.ti.com.cn/cn/lit/ds/symlink/ads1015.pdf (accessed on 10 May 2017).

[66]   F. Attivissimo, A. Cataldo, L. Fabbiano, N. Giaquinto, "Systematic errors and measurement uncertainty: An experimental approach", Measurement: Journal of the International Measurement Confederation, vol. 44, 2011, pp. 1781-1789.

[67]   F. Attivissimo, N. Giaquinto, M. Savino, "Worst-case uncertainty measurement in ADC-based instruments", Computer Standards and Interfaces, vol. 29, 2009, pp. 5-10.

[68]   Dà-Jiāng Innovations Science and Technology Co., Ltd (DJI). 2212 – 920 KV - Brushless Motor for Quadcopter/Multirotor/Drone. Available online: https://www.robomart.com/account/product2pdf?productid=1081 (accessed on 10 May 2017).

[69]   Dà-Jiāng Innovations Science and Technology Co., Ltd (DJI). E300 - Optoisolated Electronic Speed Control. Available online: http://www.dji.com/e300/spec (accessed on 10 May 2017).

[70]   G. Andria, A. D'orazio, A. Lay Ekuakille, M. Moretti, P. Pieri, F. Tralli, M. Tropeano, "Accuracy Assessment in Photo Interpretation of Remote Sensing ERS-2/SAR Images", 17th IEEE - IMTC2000, Baltimore, USA, 1-4 May 2000, pp. 392-394.

[71]   G. Andria, A. D'orazio, A. Lay Ekuakille, M. Notarnicola, "Modelling Study in Remote Sensing of Air Pollution Measured Data", 17th IEEE - IMTC2000, Baltimore, USA, 1-4 May 2000, pp. 782-785.